Figures and figure supplements

Untwisting the *Caenorhabditis elegans* embryo

Ryan Patrick Christensen *et al*

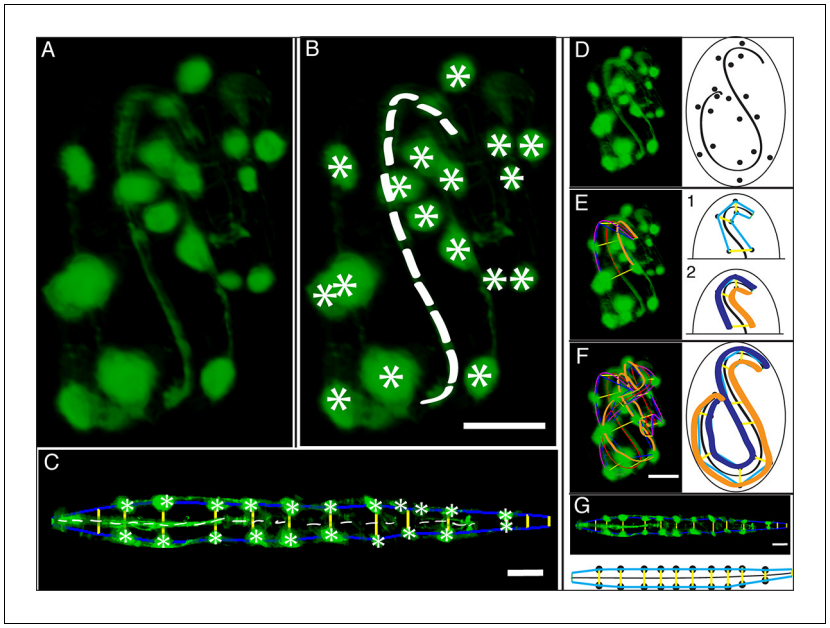

Figure 1. Key steps in worm untwisting. (**A**) An image of a threefold embryo in the twisted state, showing the untwisting markers. (**B**) The same image as in (**A**) with the untwisting markers labeled. Asterisks mark seam cell nuclei, and the dashed line indicates the midline marker. (**C**) The same embryo as in (**A**, **B**), after untwisting. Asterisks and dashed line as in **B**. (**D–F**) Further detail lattice creation and splines that model embryo. (**D**) Left: same embryo volume as in (**A**). Right: accompanying schematic showing the seam cell nuclei in the twisted embryo (black circles) and midline (interior black line). (**E**) Lattice creation. As diagrammed in right schematic, parts (1) and (2), the user adds points to create a lattice (blue and yellow lines). After the lattice is built, the algorithm generates splines defining the edges of the worm (orange and purple lines) automatically. The midline is also defined with a spline (red line at left). (**F**) The embryo volume and accompanying schematic showing a completed lattice and model. (**G**) The embryo volume and accompanying schematic after untwisting. All scale bars: 10 μm.
DOI: 10.7554/eLife.10070.003

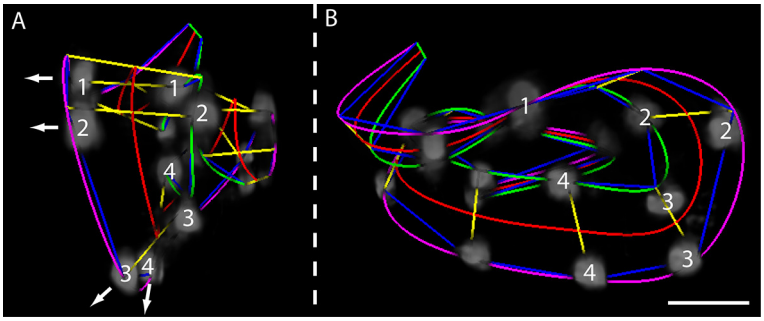

Figure 1—figure supplement 1. Helical twisting in the nematode embryo. (**A**) Evidence for helical twisting, highlighted on four pairs of consecutive seam cell nuclei. If no helical twisting occurs, yellow lines (connecting seam cell nucleus pairs) should appear parallel to each other when sighting down the midline of the worm (red line). If helical twisting is present, yellow lines should appear to twist about the midline. Arrows denote the direction of lines for four pairs of consecutive seam cell nuclei: note obvious and apparent angular twist between pairs 1 and 4. (**B**) Side view showing same data as in (**A**). As before, nuclei pairs 1 and 4 appear in close to perpendicular orientation to each other, despite the roughly parallel midline. Scale bar: 10 μm.
DOI: 10.7554/eLife.10070.004

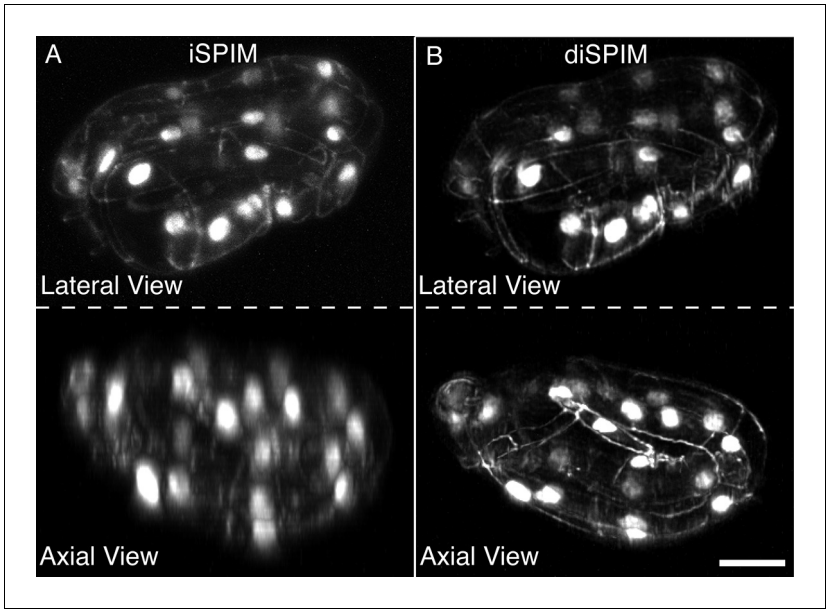

Figure 1—figure supplement 2. DiSPIM is useful in identifying landmarks in the twisted embryo. Coarse features such as seam cell nuclei are visible in single view iSPIM (**A**), but finer features such as junctions between hypodermal cells labeled with DLG-1::GFP are better resolved in the diSPIM (**B**), particularly in the axial direction (lower row). Scale bar: 10 μm. diSPIM, dual-view Selective Plane Illumination Microscopy; iSPIM, inverted Selective Plane Illumination Microscopy.

DOI: 10.7554/eLife.10070.005

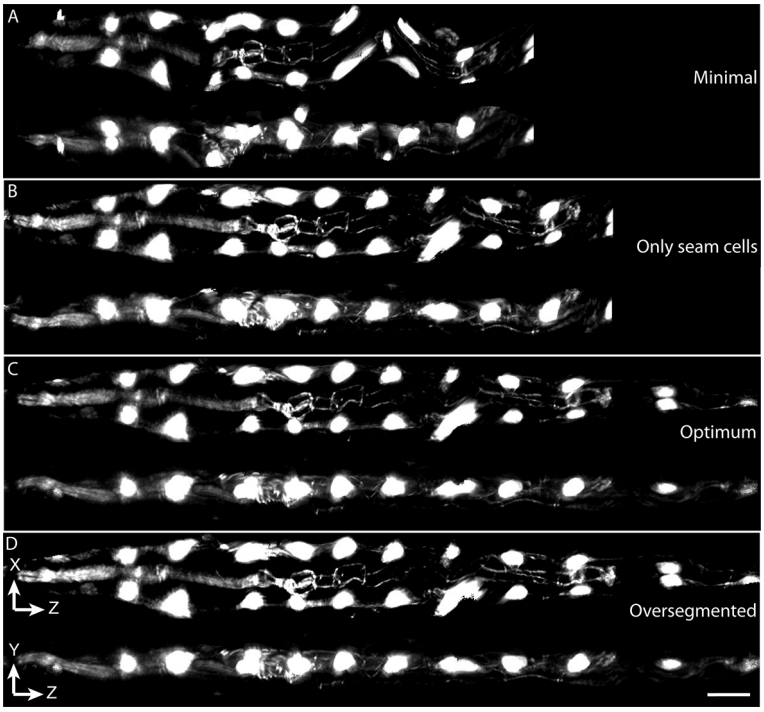

Figure 1—figure supplement 3. Effects of lattice point number on untwisting results. (**A**) XZ and YZ views of an untwisted worm embryo using a lattice comprised of every other seam cell nucleus, a total of 12 points. This lattice fails to capture bends in the animal and does not create smooth left and right edges in the untwisted worm embryo. (**B**) Same as (**A**) but using a lattice built with all seam cell nuclei and the nose, a total of 22 points. This lattice still fails to capture some bends in the worm, and the extension of the tail. (**C**) Same as (**A**) but using a lattice built with all seam cell nuclei as well as additional points in highly bent regions in the worm embryo, plus a pair of points marking the tail, for a total of 28 points. Bends are accurately captured in the resulting untwisted volume. (**D**) Several additional lattice points were added to the lattice in (**C**), along the edges of the animal, for a total of 36 points. No noticeable improvements are apparent. Scale bar: 10 μm.
DOI: 10.7554/eLife.10070.006

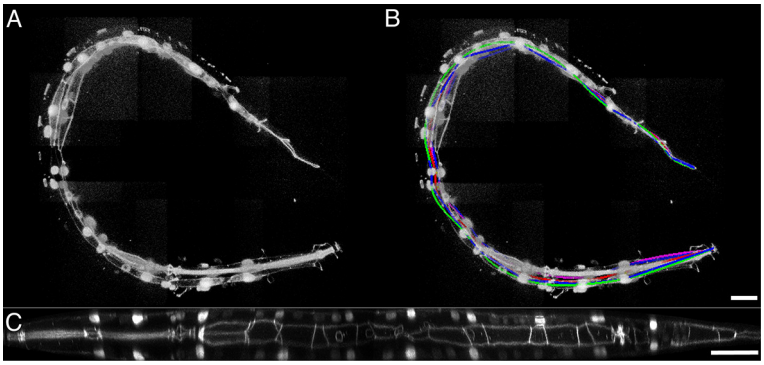

Figure 1—figure supplement 4. Untwisting a larval nematode. (**A**) The twisted L2 larval volume displayed in the MIPAV volume renderer. (**B**) The twisted L2 larva after lattice-building. (**C**) The L2 larval worm after untwisting. See also ***Video 7***. MIPAV, Medical Image Processing, Analysis, and Visualization

DOI: 10.7554/eLife.10070.007

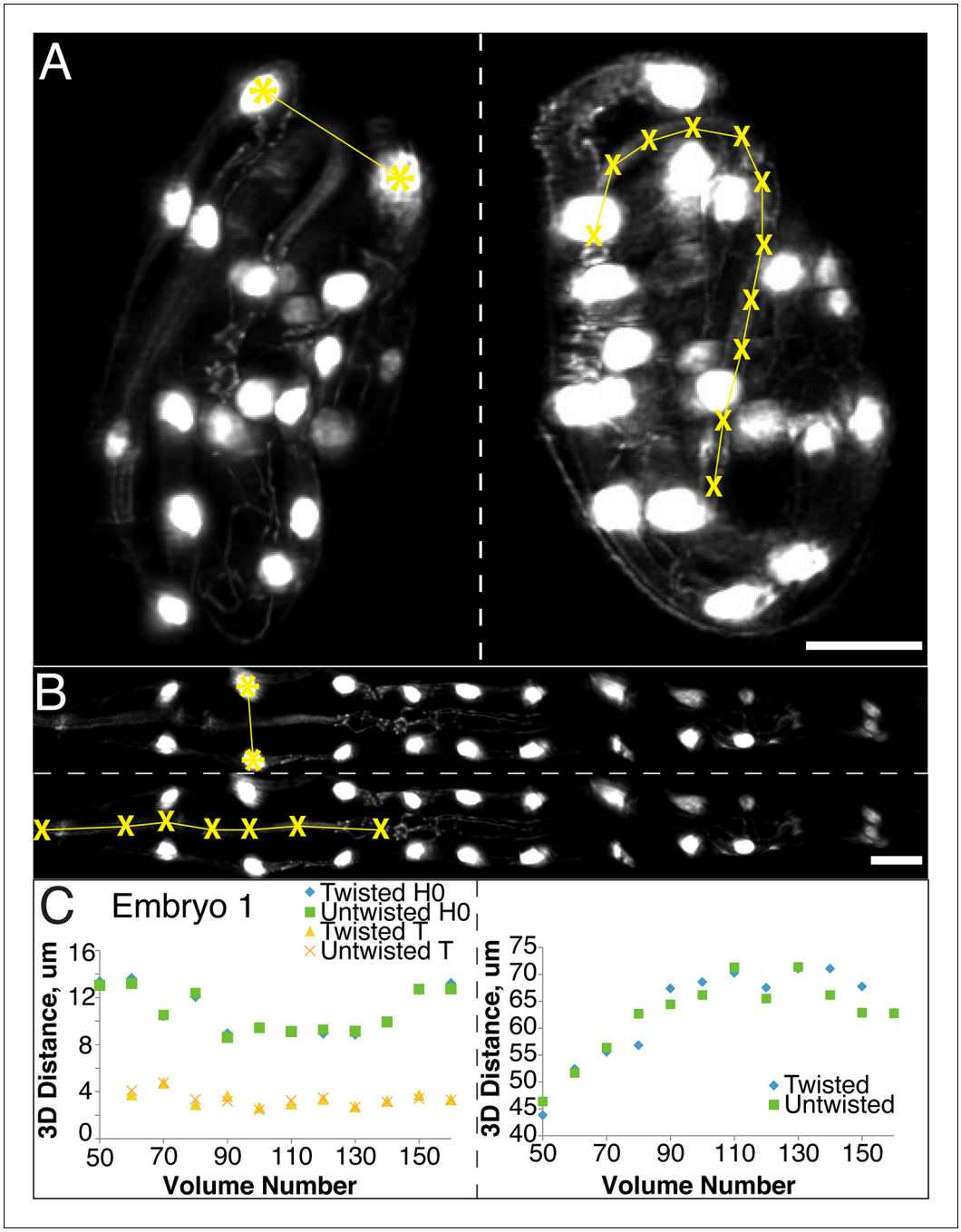

Figure 2. The untwisting algorithm accurately preserves embryo dimensions. Distances between seam cell nuclei (left) and pharyngeal lengths (right) were compared in twisted (**A**) and untwisted (**B**) worm embryos. All scalebars: 10 μm. (**C**) Comparative 3D distance measurements of seam cell nuclei pairs H0 and T (left graphs) and pharyngeal lengths (right graphs) for one representative embryo (a comparison across six different embryos is presented in ***Figure 2—figure supplement 1***). In all cases, distance measurements in the twisted case are within 5 μm of distance measurements in the untwisted case.

DOI: 10.7554/eLife.10070.009

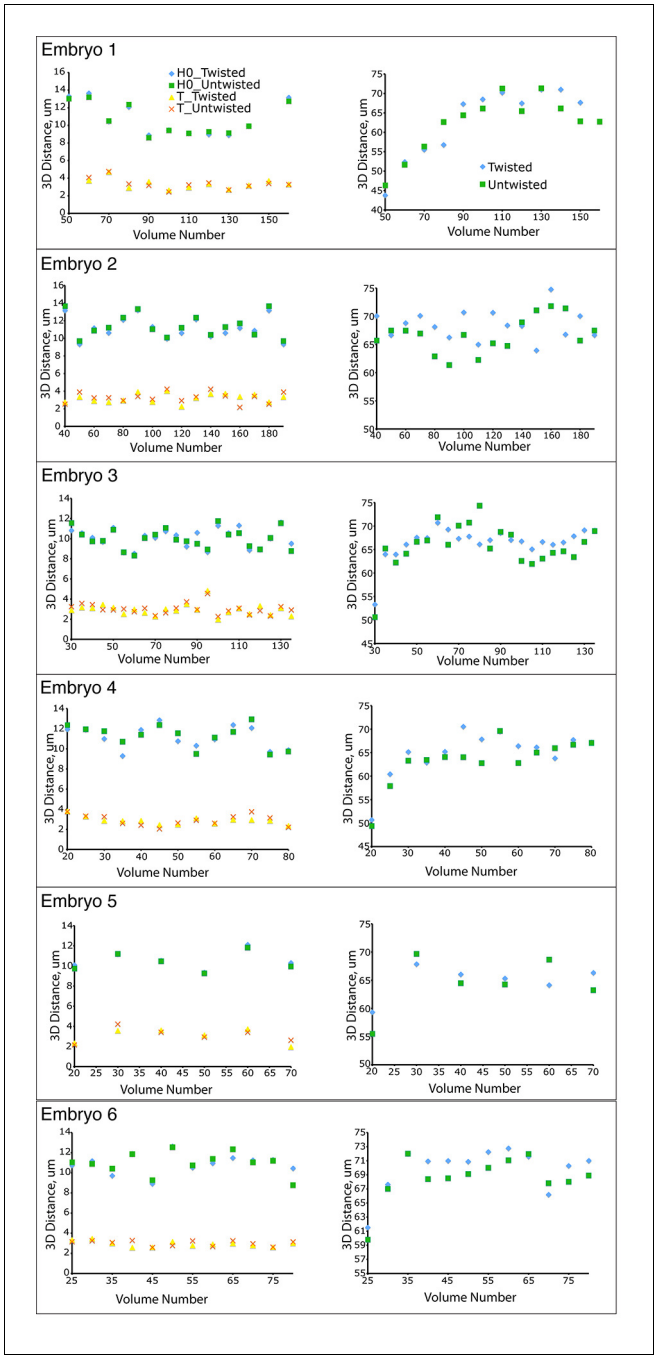

Figure 2—figure supplement 1. Untwisting does not systematically alter worm morphology Comparative 3D distance measurements of seam cell nuclei pairs H0 and T (left graphs) and pharyngeal lengths (right graphs) for six embryos. In all cases, distance measurements in the twisted case are within 10 μm of distance measurements in the untwisted case.

DOI: 10.7554/eLife.10070.010

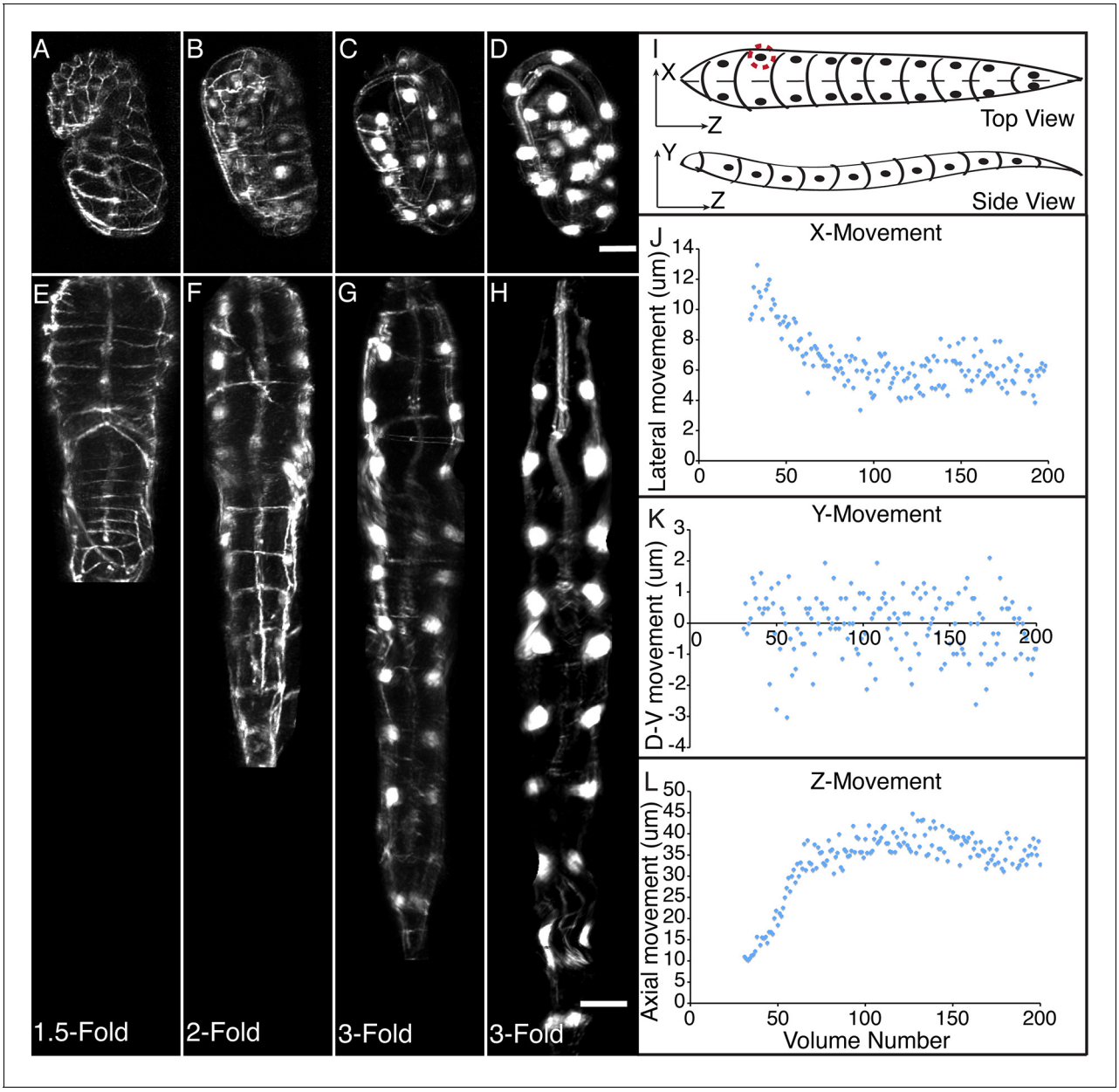

Figure 3. Morphological changes in embryonic development, as unveiled by untwisting algorithm. Selected volumetric timepoints pre (**A–D**) and post (**E–H**) untwisting, with canonical state of embryo indicated at bottom. See also ***Video 2***. (**I**) Cartoon of untwisted embryo, indicating coordinate system. (**J–L**) X, Y, and Z movements of circled seam cell nucleus in (**I**). Measurements are indicated relative to the animal's nose, fixed as the origin in all untwisted datasets. All scalebars: 10 μm.

DOI: 10.7554/eLife.10070.011

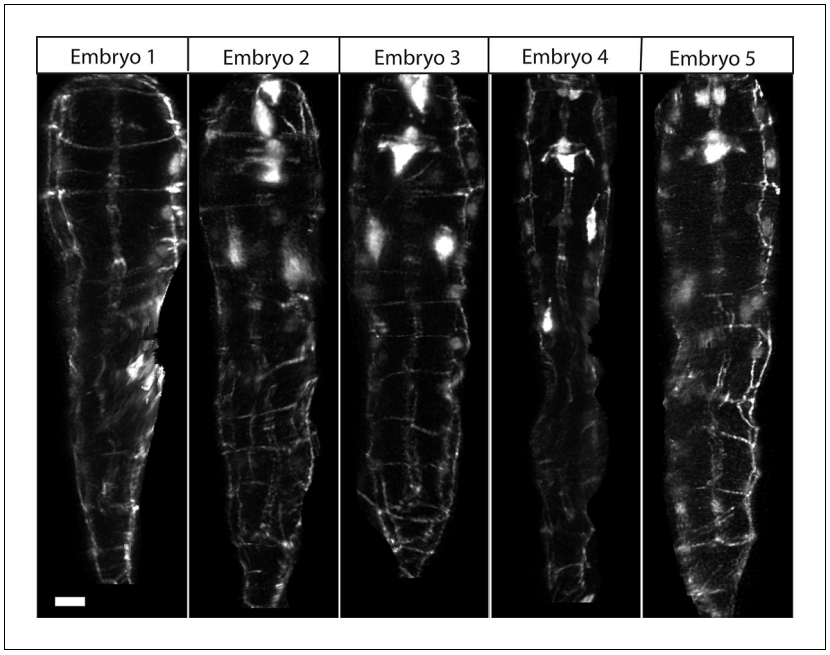

Figure 3—figure supplement 1. Comparison of untwisted 1.5-fold embryos after shifting. Comparative timepoints were selected based on the H1R seam cell shifts. Max projections of volumetric images are shown. Note the underlying similarity in overall shape across animals. Scalebar: 5 μm.
DOI: 10.7554/eLife.10070.012

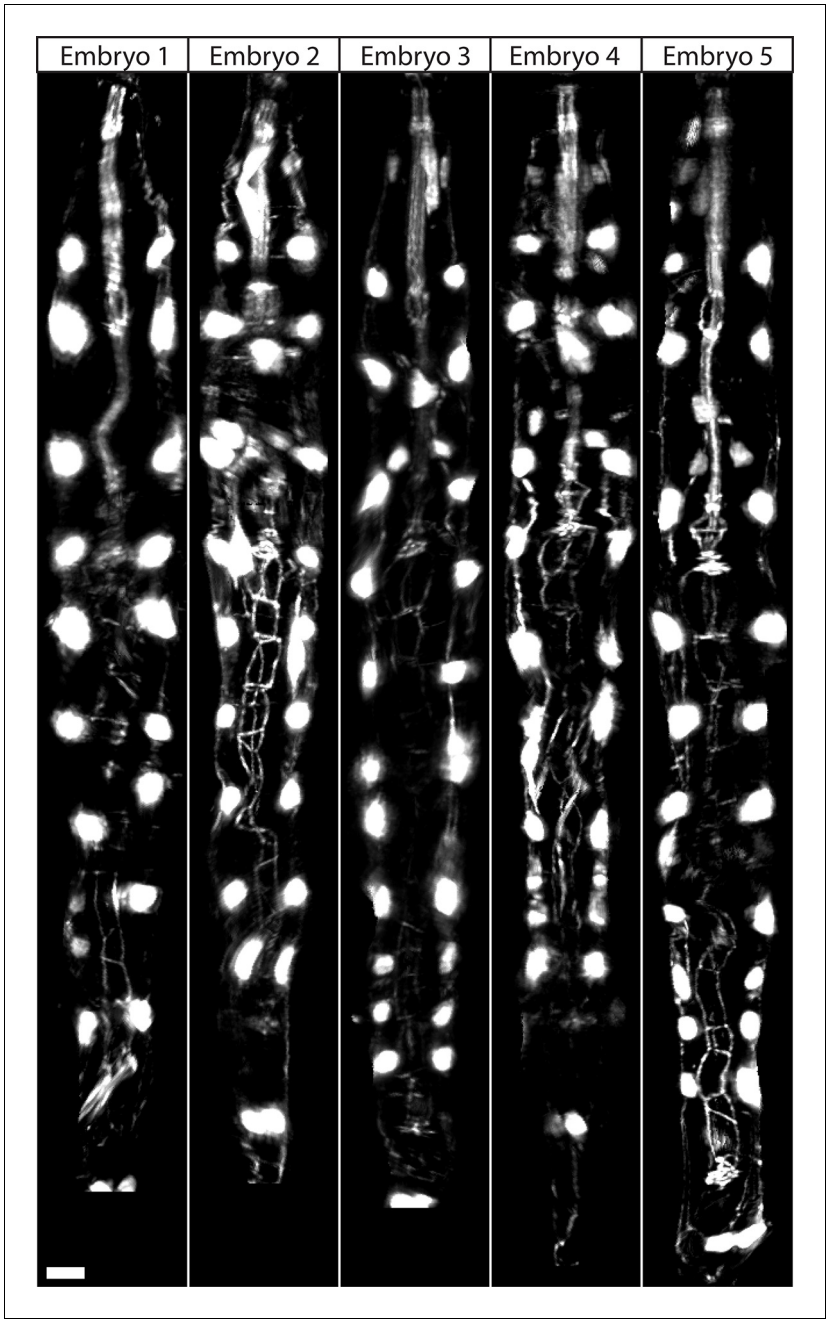

Figure 3—figure supplement 2. Comparison of threefold embryos after shifting. Comparative timepoints were selected based on the H1R seam cell shifts. Max projections of volumetric images are shown. Note the underlying similarity in overall shape and seam cell positions across animals. Scalebar: 5 μm.
DOI: 10.7554/eLife.10070.013

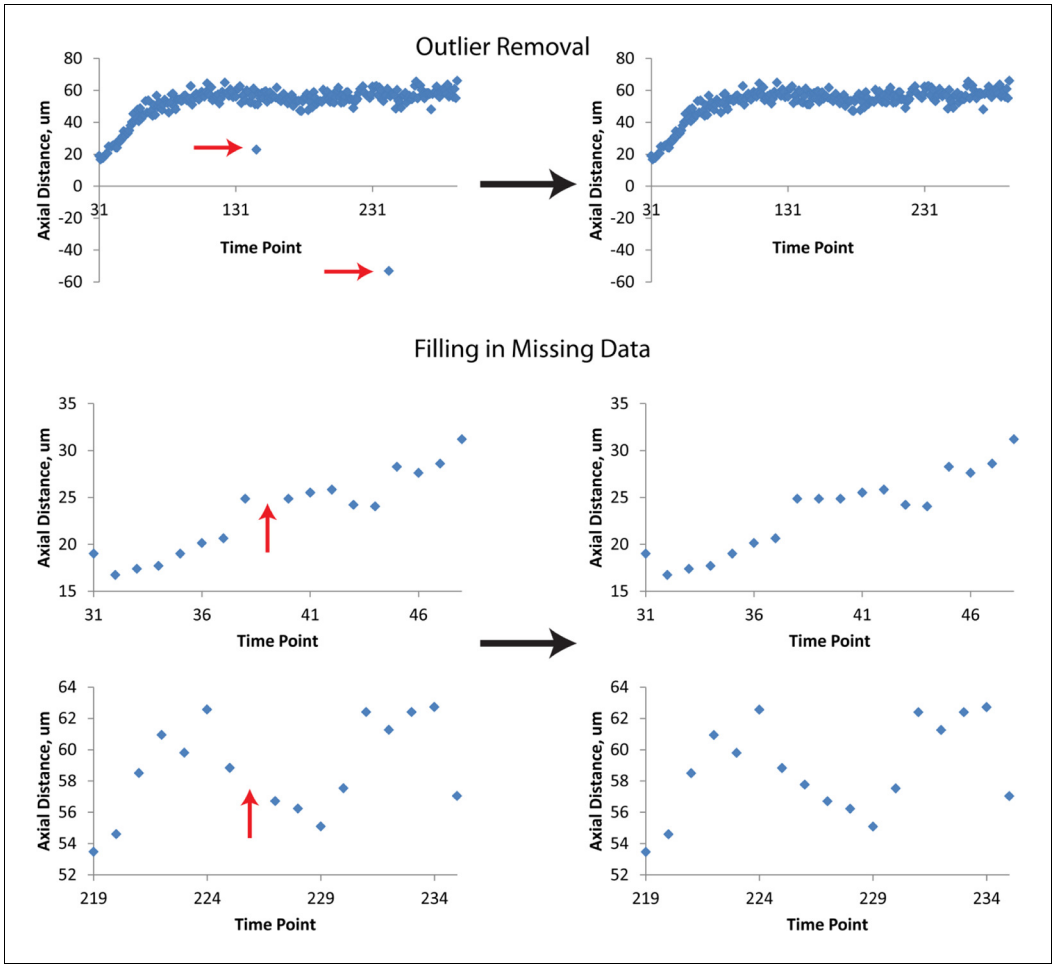

Figure 3—figure supplement 3. Data Post-processing. Before fitting, raw data are treated to remove obvious outliers (top row) and to fill in missing data (mid, bottom rows). In both cases, outliers and 'gaps' within data are found manually, and replaced by averaging the data points immediately preceding or following the outlier or gap. Examples of raw data prior to this linear interpolation are shown at left, and examples of processed data at right. The example axial distance data shown here are derived from seam cell 3. Red arrows indicate outliers or gaps. Data shown are from the left H2 seam cell nucleus.

DOI: 10.7554/eLife.10070.014

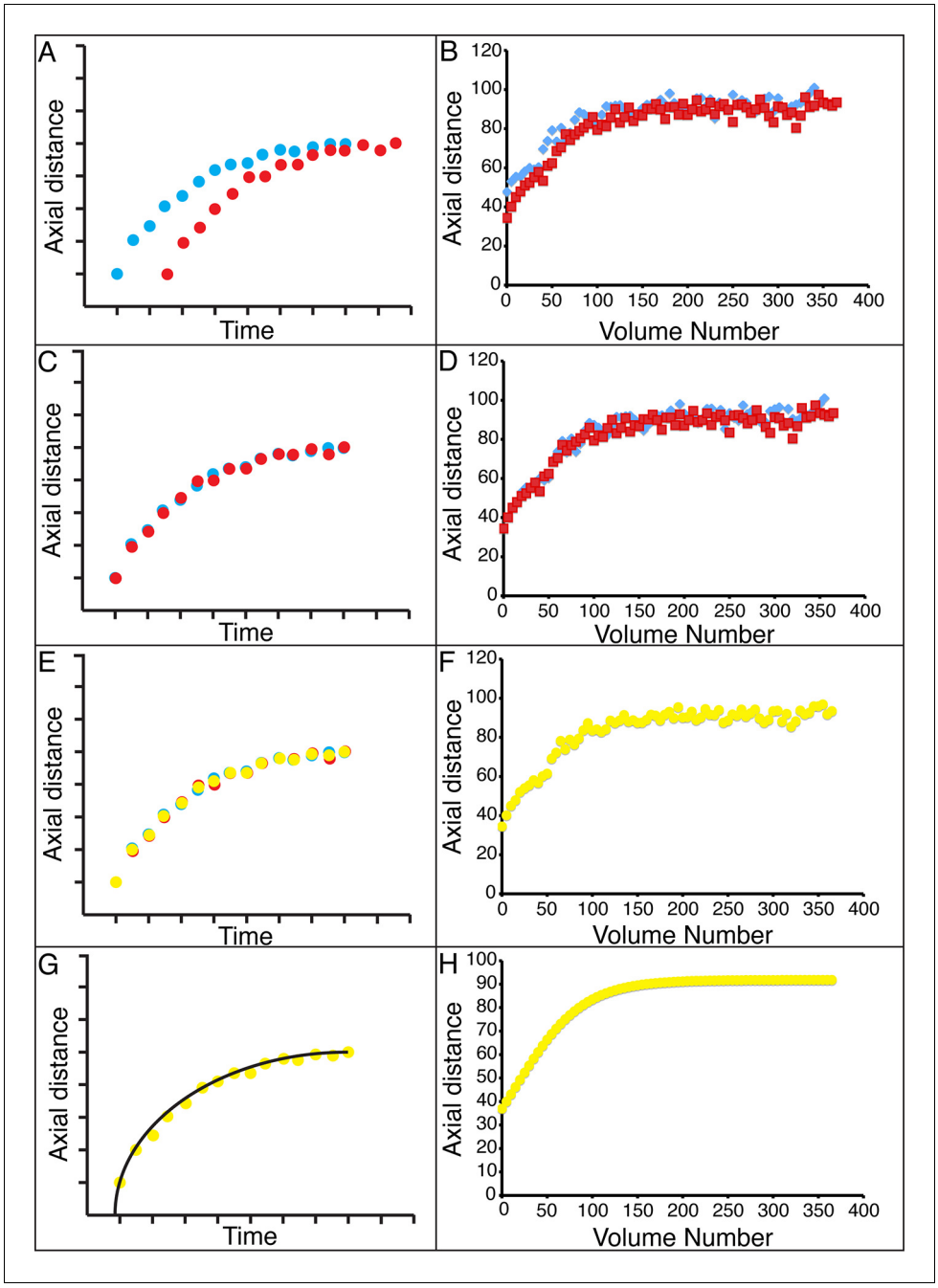

Figure 4. Alignment of data from different embryos. (**A**,**B**) Axial seam cell nuclear trajectories from different embryos are similar in shape, but shifted in time. (**C**,**D**) Shifting in time aligns the trajectories. (**E**, **F**) Averaging the shifted trajectories. (**G**, **H**) Fitting the shifted trajectories. Left graphs: cartoon schematic, Right graphs: data. For clarity, we have shown the shifting, averaging, and fitting process for two embryos, but note that to construct our 'composite' model of seam cell nucleus behavior we have applied the same process to five embryos (see '**Materials and methods**' for further details).

DOI: 10.7554/eLife.10070.016

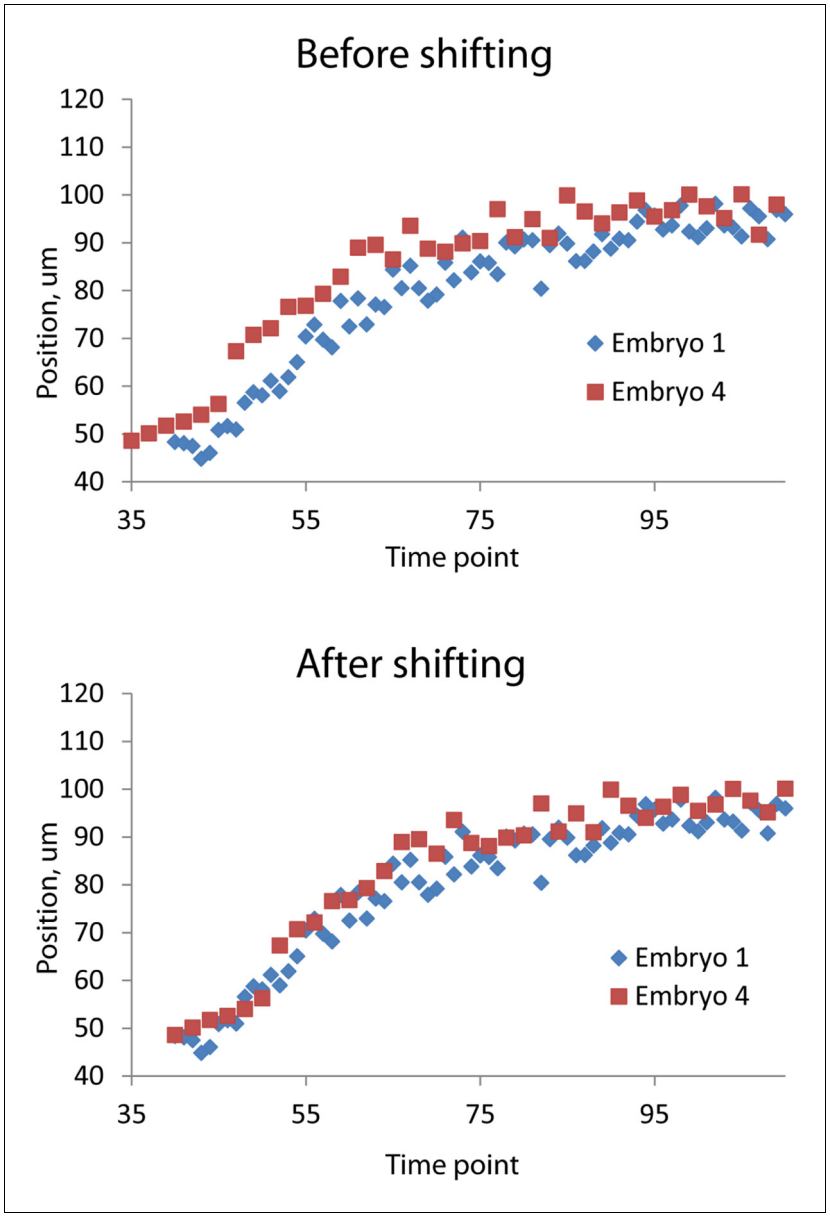

Figure 4—figure supplement 1. Temporal alignment of embryo data. Data from two embryos are shown before (top) and after (bottom) temporal alignment. The data derived from embryo 4 was shifted 5 timepoints to the right, following the procedure described in '**Materials and methods**'. Data shown are the z positions from the right V3 seam cell nucleus. Only a portion of the data, at early timepoints, is shown to highlight the shifting procedure.
DOI: 10.7554/eLife.10070.017

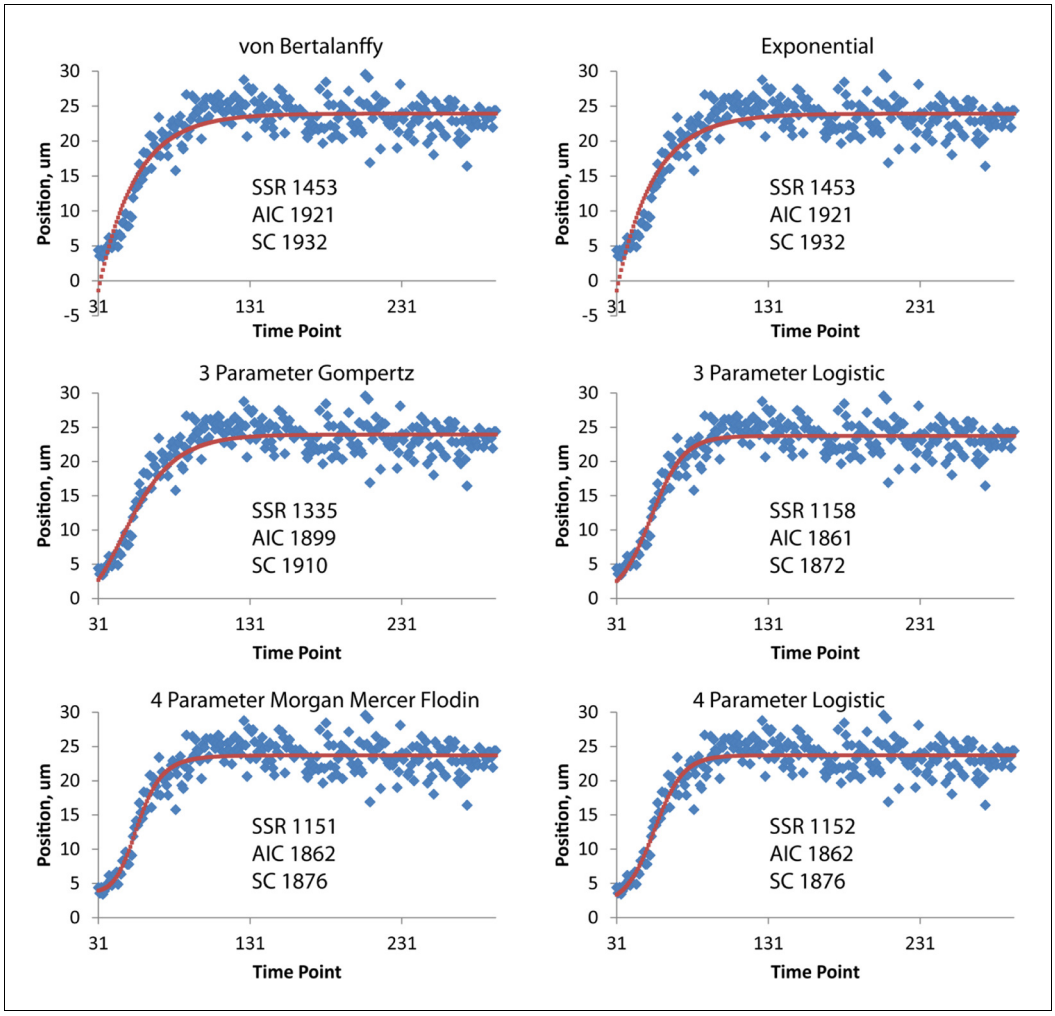

Figure 4—figure supplement 2. Different fits for axial displacement. Different fitting models (see also ***Table 2***) for embryonic axial displacement are plotted (red curves), against raw data (blue diamonds). Also shown on each plot are quantitative measures of goodness of fit: the squared sum of residuals (SSR), the Akaike Information Criterion (AIC), and the Schwarz Criterion (SC). Of the three-parameter fits, the three-parameter logistic provides the best overall fit, both from visual inspection and quantitatively (lowest SSR, AIC, and SC scores). The four-parameter Morgan Mercer Flodin and Logistic curves show slightly better qualitative fits, especially at early time points, but require careful tuning of the initial parameters to converge. For all axial displacement data shown elsewhere in the paper, the three-parameter logistic curve was used as a fitting function. Although the axial displacement data shown here are derived from the left seam cell nucleus H0, we observed the same trends for all seam cells.

DOI: 10.7554/eLife.10070.018

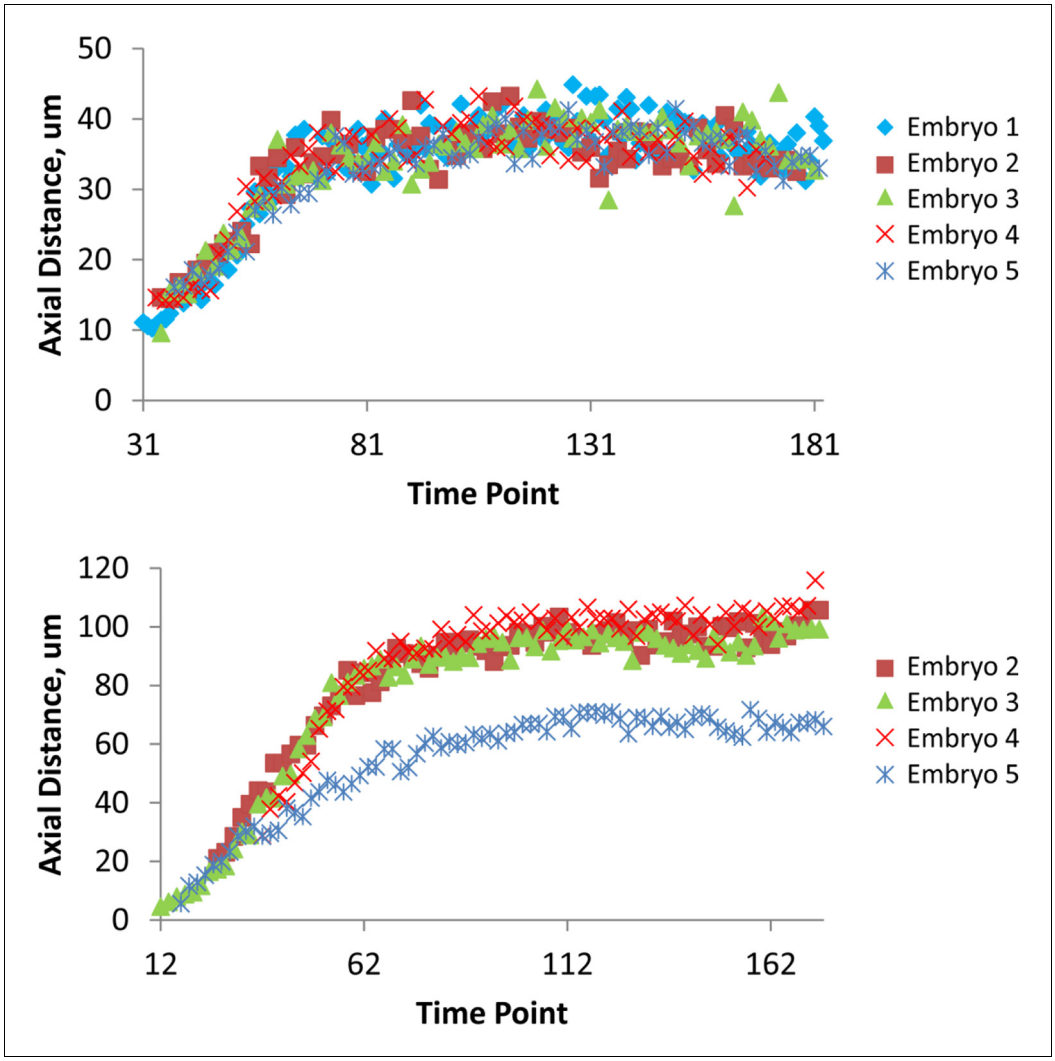

Figure 4—figure supplement 3. Variability in axial distance amongst different embryos. Comparisons in axial position vs. time for a seam cell nucleus (right H1, upper graph) and for CANL (lower graph). For most nuclei, as in the upper graph, positions were stereotyped to within 4.6 μm (as quantified by $<<\sigma_Z>_{time}>_{seam\ cell}$; see also '**Materials and methods**'). As indicated in the lower graph, we noticed CANs in embryo 5 traveled a shorter distance than in other embryo datasets (resulting in a larger value of $<\sigma_Z>_{time}$ for CANL, see ***Supplementary file 2***). Data are shown after applying the shifting procedure described in '**Materials and methods**'.

DOI: 10.7554/eLife.10070.019

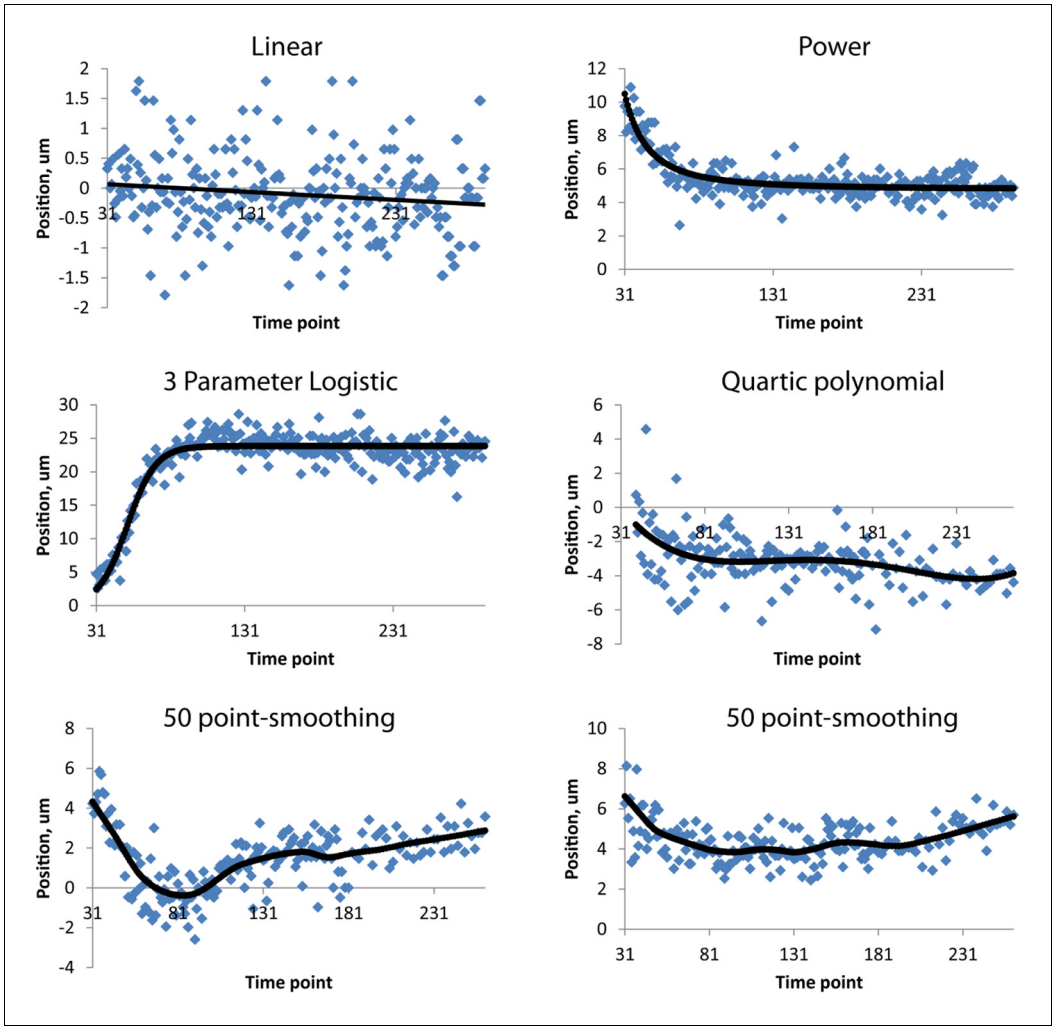

Figure 4—figure supplement 4. Fits used in this paper. Examples of raw, averaged data (derived from 4 to 5 embryos, blue dots) and fits (black lines). Linear, power, and three-parameter logistic curve examples were taken from the right H0 seam cell nucleus, the quartic polynomial example from AIYL, and the smoothing fits from CANR. See also ***Table 1***. Note the different ranges in ordinate axes.

DOI: 10.7554/eLife.10070.020

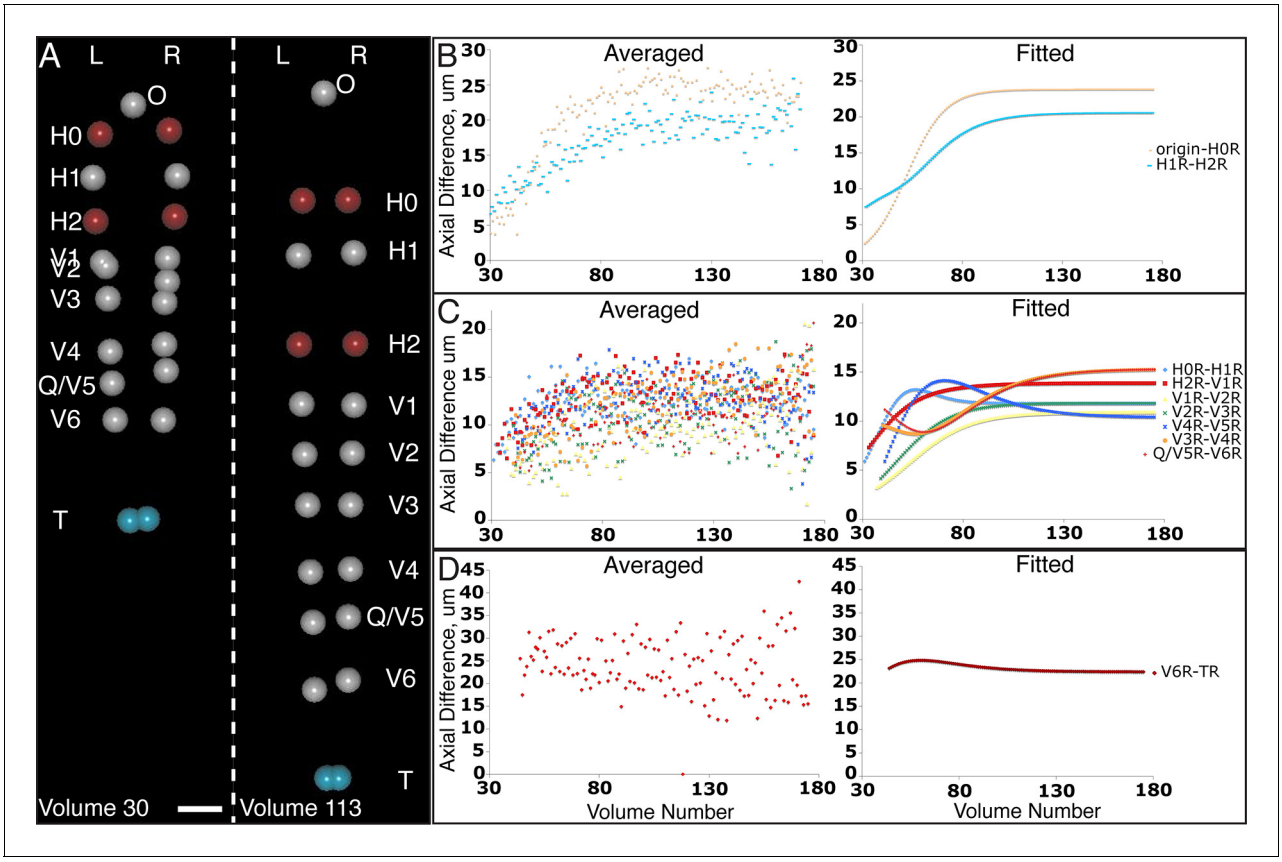

Figure 5. Variability in seam cell nucleus axial movement in the elongating embryo. (**A**) Snapshots of the elongating embryo near start (Volume 30, left) and end (Volume 113) of elongation. Seam cell nuclei volumes are indicated as filled spheres, L/R axes are as indicated, seam cell nuclear identities indicated at the side of each snapshot, as is the origin (nose, 'O'). See also ***Videos 3***,***4***. Scalebar: 10 μm. (**B**–**D**) Axial differences over the course of elongation between adjacent seam cell nucleus pairs, sorted into greatest (**B**), intermediate (**C**), and least (**D**) bins, corresponding to red, gray, and blue coloring indicated in (**A**). Left graphs: raw, averaged data (as in ***Figure 4E***, ***4F***). Right graphs: fitted data (as in ***Figure 4G***, ***4H***).
DOI: 10.7554/eLife.10070.025

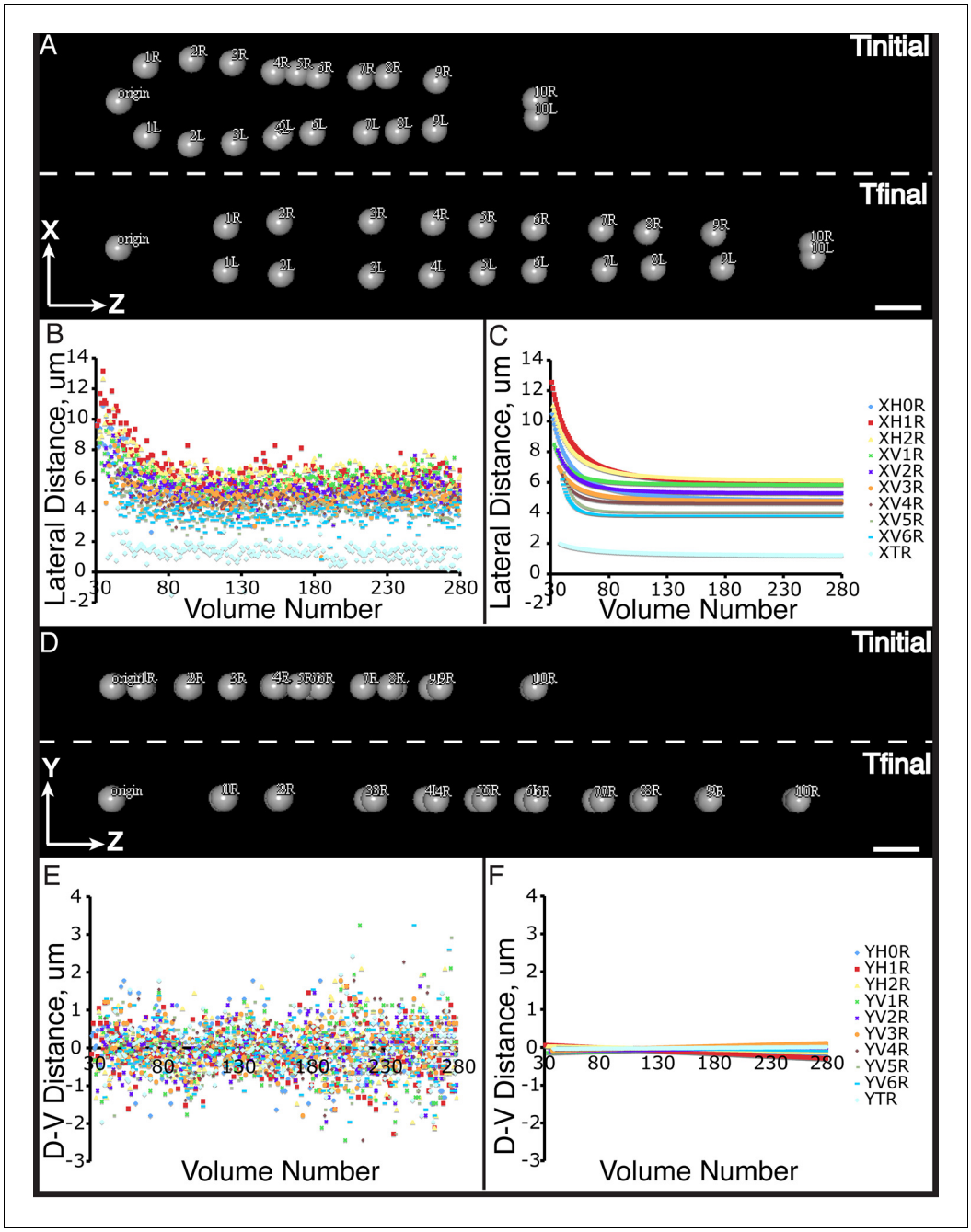

Figure 5—figure supplement 1. Seam cell nucleus XY movement in the elongating embryo. (**A**–**D**) Snapshots of the elongating embryo at start (above dashed line) and end (below dashed line) of elongation, as shown in lateral (X motion, **A**) and dorsal-ventral (Y motion, **C**) views. Distances from the origin in X (**B**, **C**) and Y (**E**,**F**) are also shown for each seam cell nucleus. Both averaged (**B**, **E**) and fitted (**C**, **F**) distances are displayed. Scalebars: 10 μm.
DOI: 10.7554/eLife.10070.026

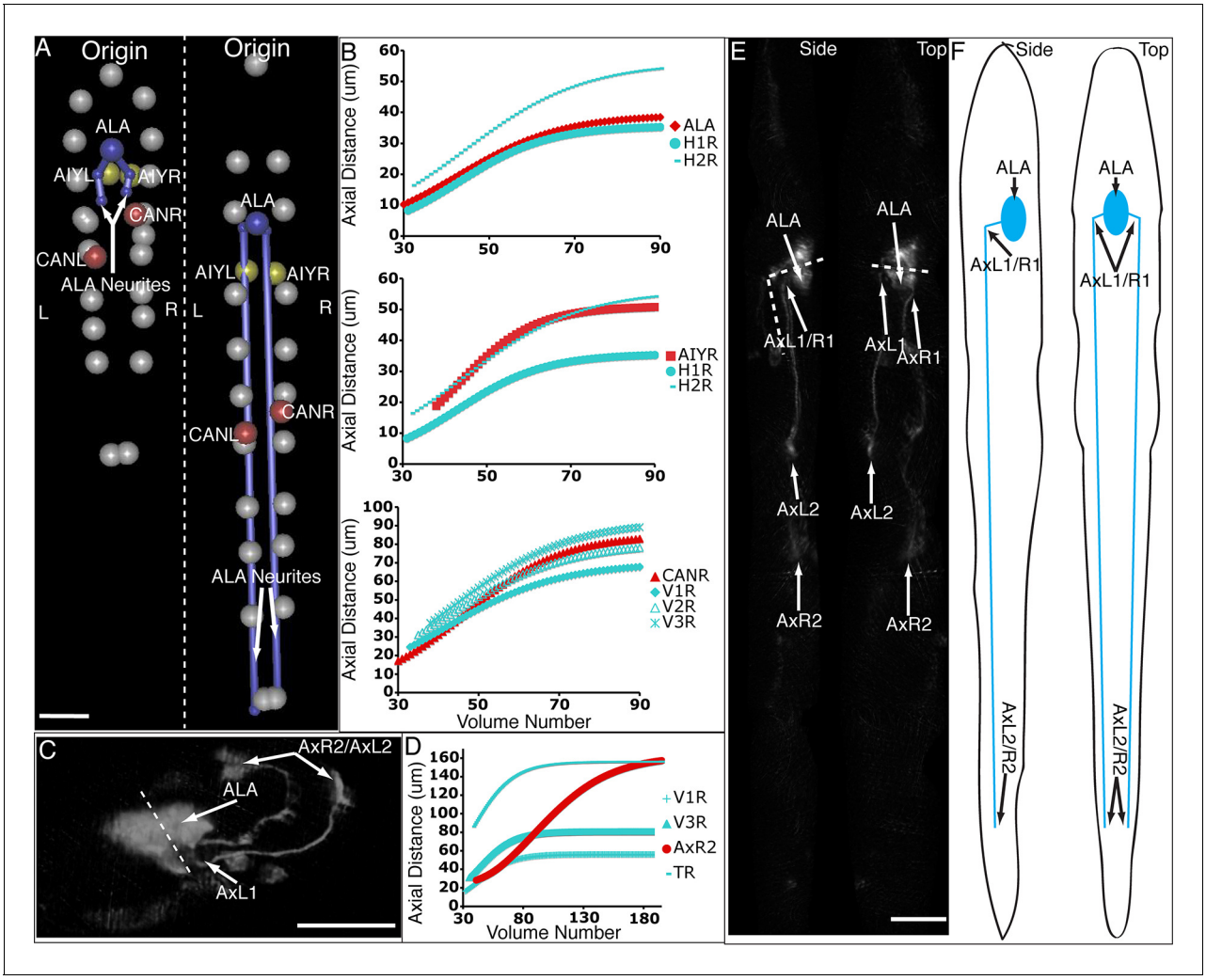

Figure 6. Neurons and neurites in the developing embryo. (**A**) Early (left) and late (snapshots) in the elongating embryo. Gray spheres: seam cell nuclei; ALA cell body: blue sphere; ALA neurites: blue lines; AIY cell bodies: yellow spheres; CAN cell bodies: red spheres. Compare to ***Videos 5,6***. (**B**) ALA (top), AIYR (middle), and CANR (bottom) axial trajectories (red curves) in relation to neighboring seam cells (blue curves). ALA and AIY cells maintain their relative position with respect to the rest of the elongating body, while CANs migrate faster than neighboring seam cells. (**C**) ALA cell body and neurite in the twisted embryo, highlighting morphological features (ALA: ALA cell body; AxL1/R1: junction between ventral and posterior neurite extension; AxL2/R2: posterior tip of the ALA neurites). (**D**) Axial trajectory of ALA neurite tip in relation to indicated seam cells. (**E**) Top and side models of ALA in untwisted reference frame, indicating neurite bend and terminus. Compare to ***Figure 6—figure supplement 2***.

DOI: 10.7554/eLife.10070.029

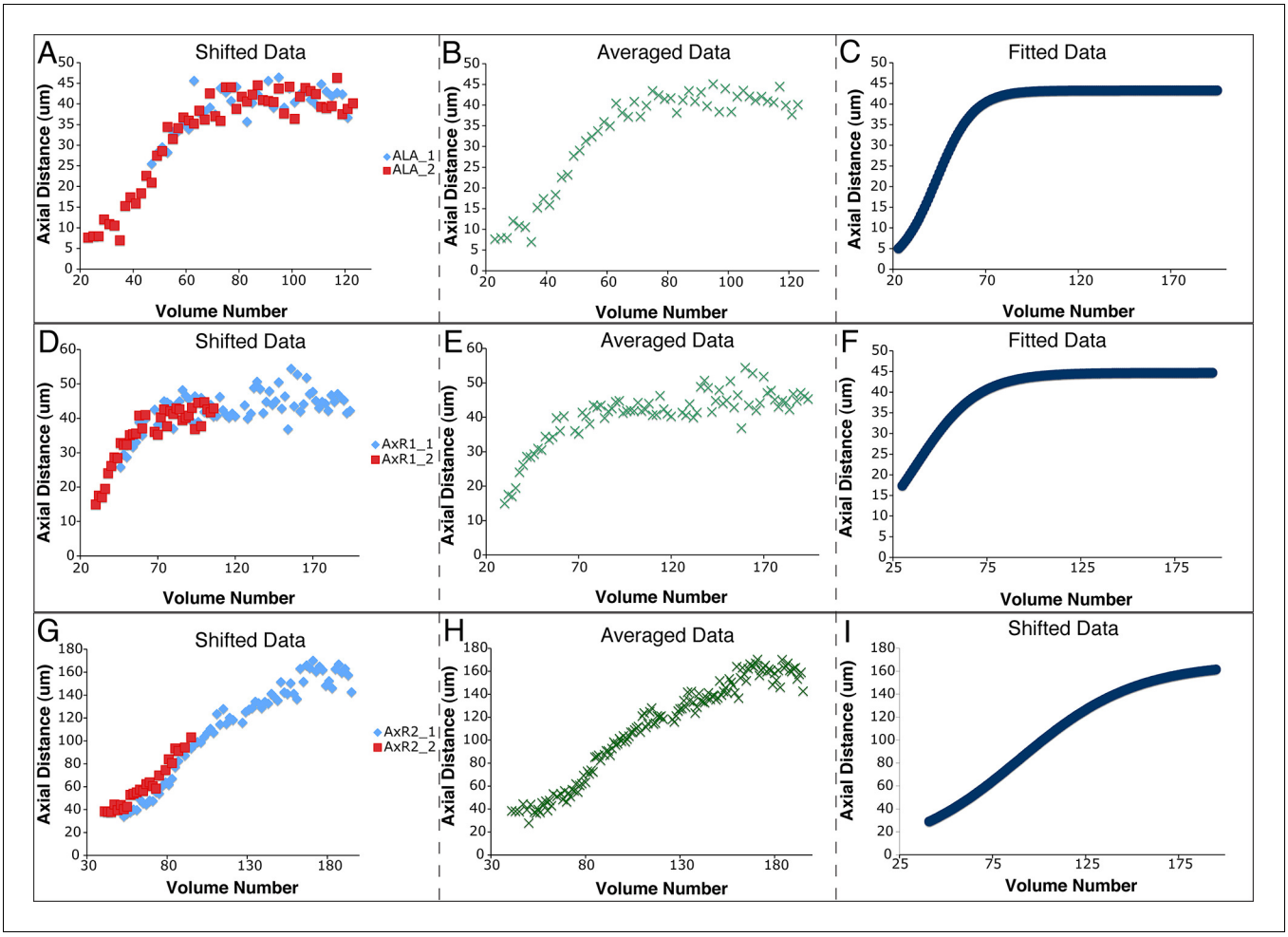

Figure 6—figure supplement 1. Shifting, averaging and fitting procedures for modeling the ALA neurite. (**A**) Axial distance (measured from the origin point) of the ALA cell body for two ALA datasets. Similar to seam cells, axial distance increases during elongation and then plateaus once elongation has finished. (**B**) ALA axial distance, derived from averaging the axial distances of the shifted ALA datasets. (**C**) A fitted curve describing axial motion of ALA, after averaging in (**B**). (**D**–**F**) Shifting, averaging, and fitting of axial motion for the AxR1 point in the ALA neurite (the position at which the ventral growth of the neurite changes to posterior growth). As there is little axial growth in this part of the neurite, axial movement mirrors that of the ALA cell body. (**G**–**I**) Shifting, averaging, and fitting of axial motion for AxR2, the tip of the posteriorly-growing ALA neurite. The posterior-ward axial extension of the neurite leads to a different pattern of axial movement than for the R1 point or the ALA cell body.

DOI: 10.7554/eLife.10070.030

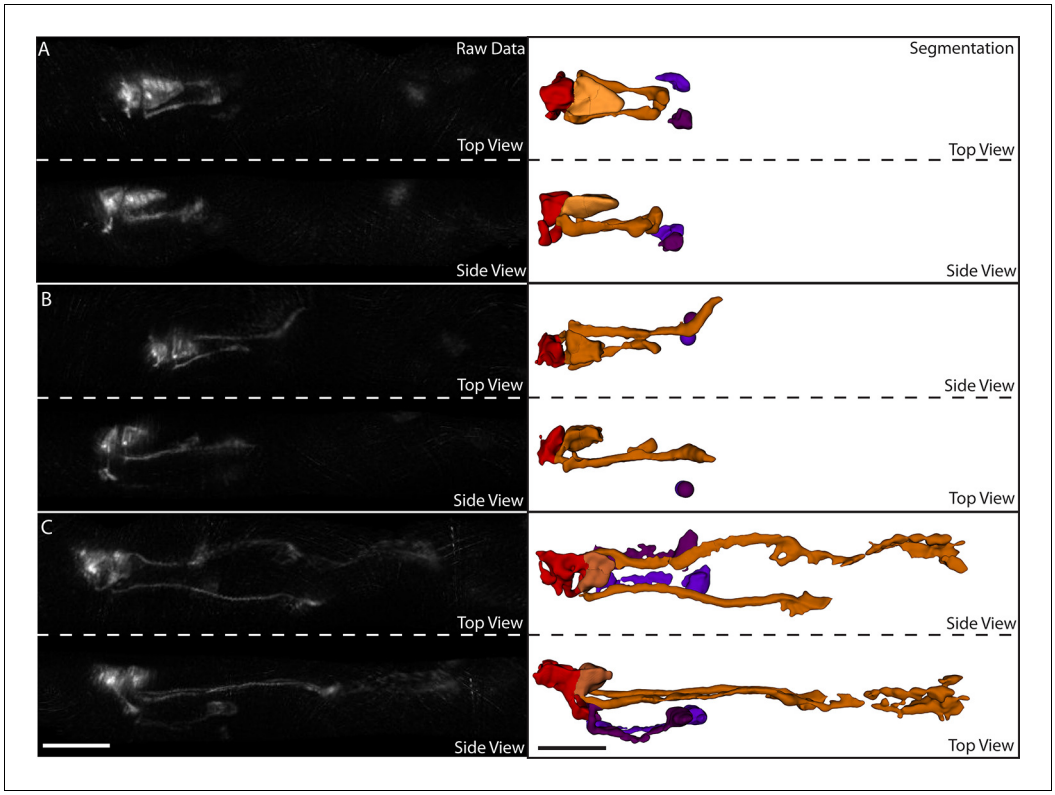

Figure 6—figure supplement 2. Segmentation of neurons and neurites in the untwisted embryo. (**A**) Exemplary data for a twofold embryo. Left column: raw data. Right column: segmented data. The red neuron is RMED, the orange neuron is ALA, and the purple neurons are the cell bodies of the AIY neurons. At this point in embryonic development, the ALA neurites have extended ventrally and begun extending posteriorly, but have not undergone much extension. (**B**) Same embryo and color-scheme as in (**A**), but now early threefold stage. More ALA neurite extension is evident. (**C**) Same as in (**B**), but at a later stage. The ALA neurites have extended approximately 1/3 of the way to the tail at this point. In addition, neurite extension can also be observed in the AIY and RMED neurons. Scalebar: 10 μm.

DOI: 10.7554/eLife.10070.031

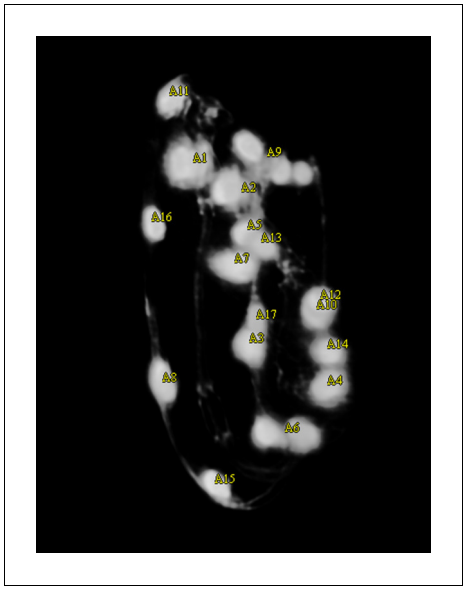

Appendix 1—figure 1. Output of the automatic seam cell nucleus detection algorithm shown before editing starts. The markers are yellow, indicating that fewer than 20 seam cell nuclei have been labeled.
DOI: 10.7554/eLife.10070.039

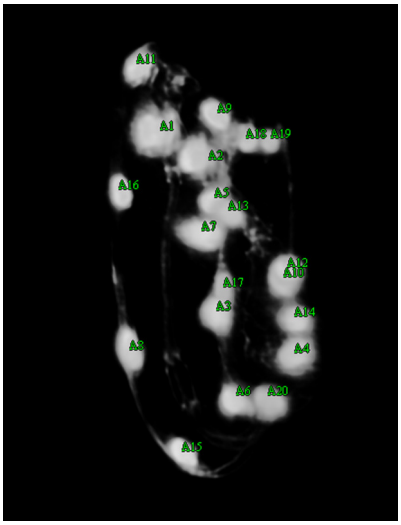

Appendix 1—figure 2. User editing. The user shifts seam cell nucleus #9 over, adds markers for both of the 10th seam cell nuclei, shifts nucleus #6 over and adds nucleus #20. There are now 20 seam cell nuclei marked, as indicated by the green color.
DOI: 10.7554/eLife.10070.040

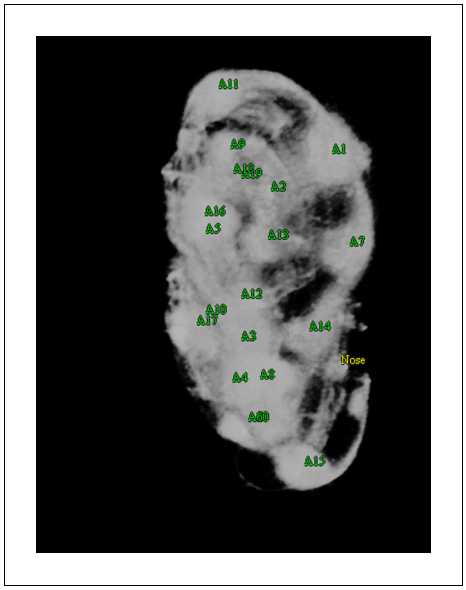

Appendix 1—figure 3. Nose labeling. The user has increased the opacity of the volume to better enhance the appearance of the nose, now labeled in yellow.
DOI: 10.7554/eLife.10070.041

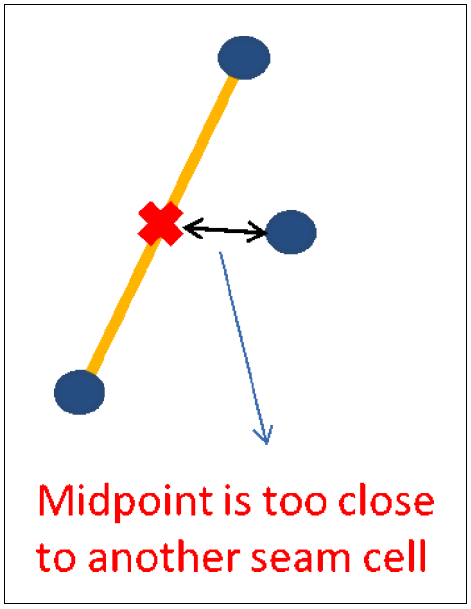

Appendix 1—figure 4. Pairing quality control. A potential pair is found, with the mid-point marked in red. A third seam cell nucleus is found closer to the mid-point than the pair, invalidating the pair.
DOI: 10.7554/eLife.10070.042

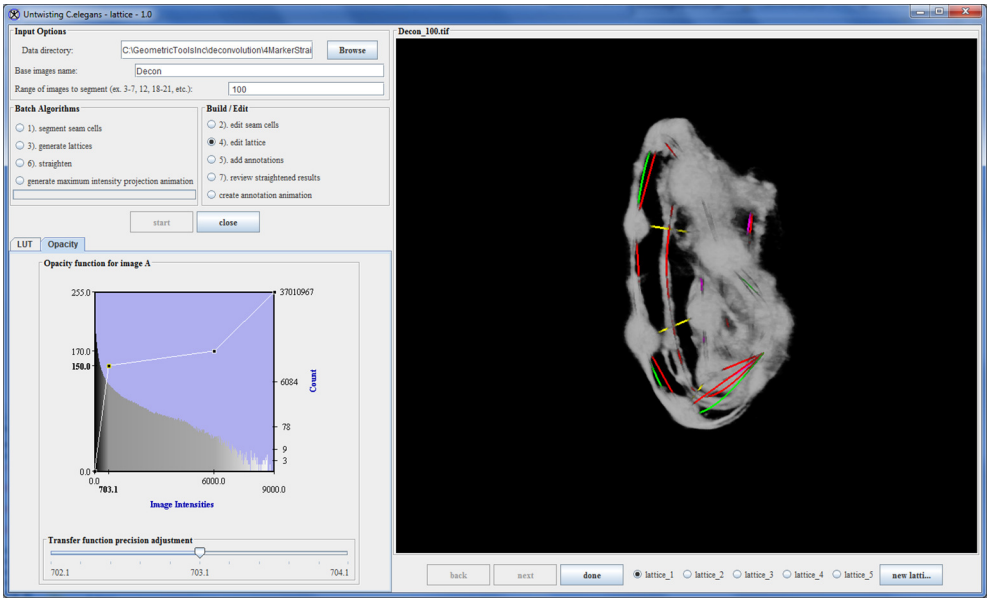

Appendix 1—figure 5. Automatic lattice-building output. The correct lattice is listed first as it had the highest rank.

DOI: 10.7554/eLife.10070.043

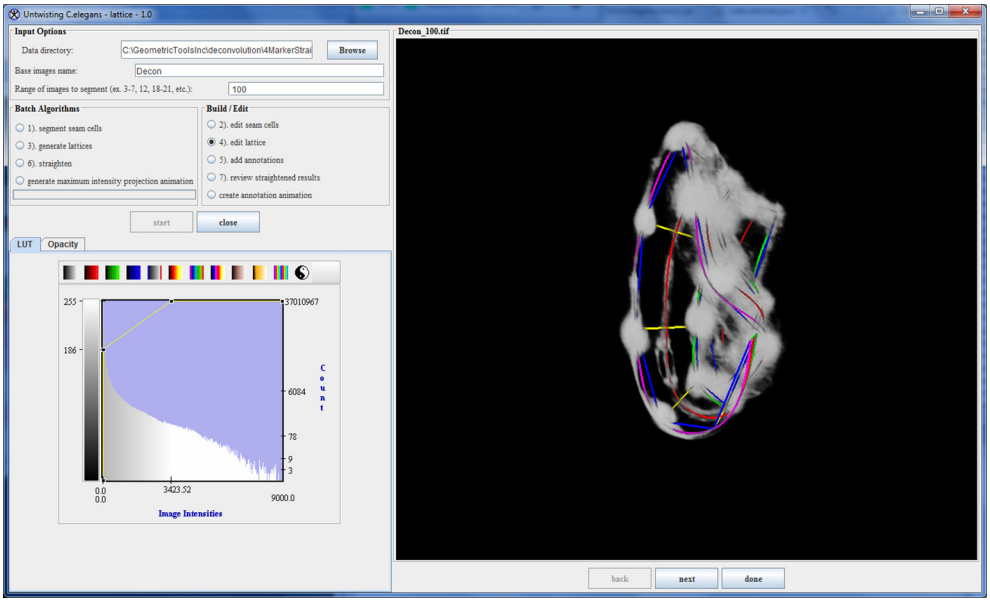

Appendix 1—figure 6. The lattice after editing by the user.
DOI: 10.7554/eLife.10070.044

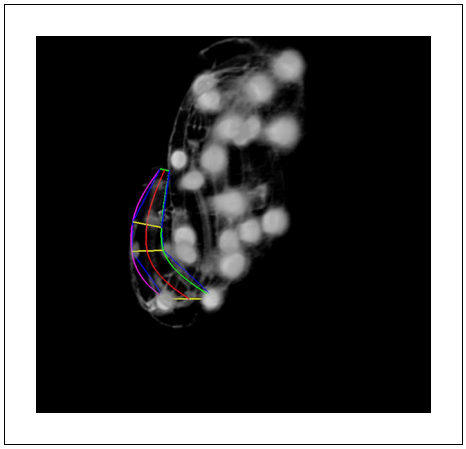

Appendix 1—figure 7. The user has started building the lattice starting at the head of the worm.
DOI: 10.7554/eLife.10070.045

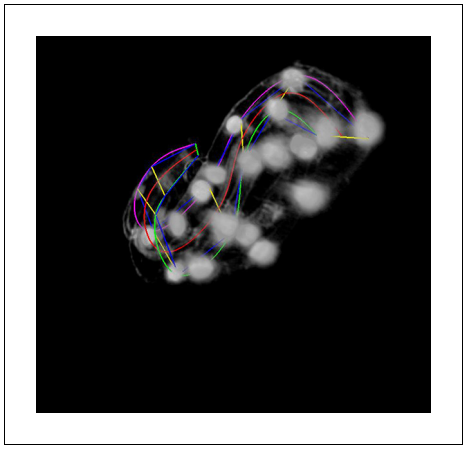

Appendix 1—figure 8. More points are added to the lattice. The user rotates the volume to get a better view during this phase. The magenta, red, and green curves represent the left- hand curve, center-line curve, and right-hand curves respectively. The curves are natural splines which are guaranteed to pass through the user-selected lattice points while minimizing bending to produce a smooth curve that matches the shape of the worm fairly accurately.
DOI: 10.7554/eLife.10070.046

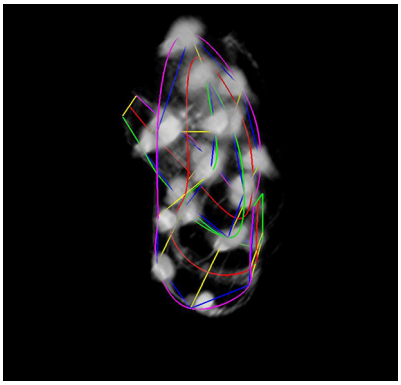

Appendix 1—figure 9. The final lattice. Each of the 10 seam-cell pairs is marked, and 8 additional pairs have been added to capture the curve of the worm.
DOI: 10.7554/eLife.10070.047

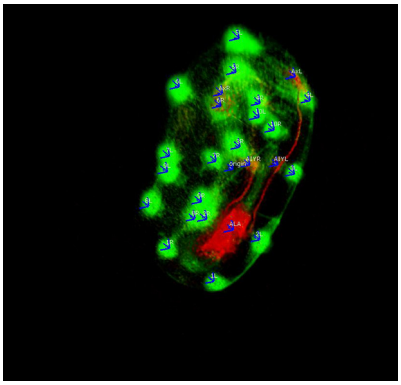

Appendix 1—figure 10. Annotations added to the worm volume labeling parts of the neuron.
DOI: 10.7554/eLife.10070.048

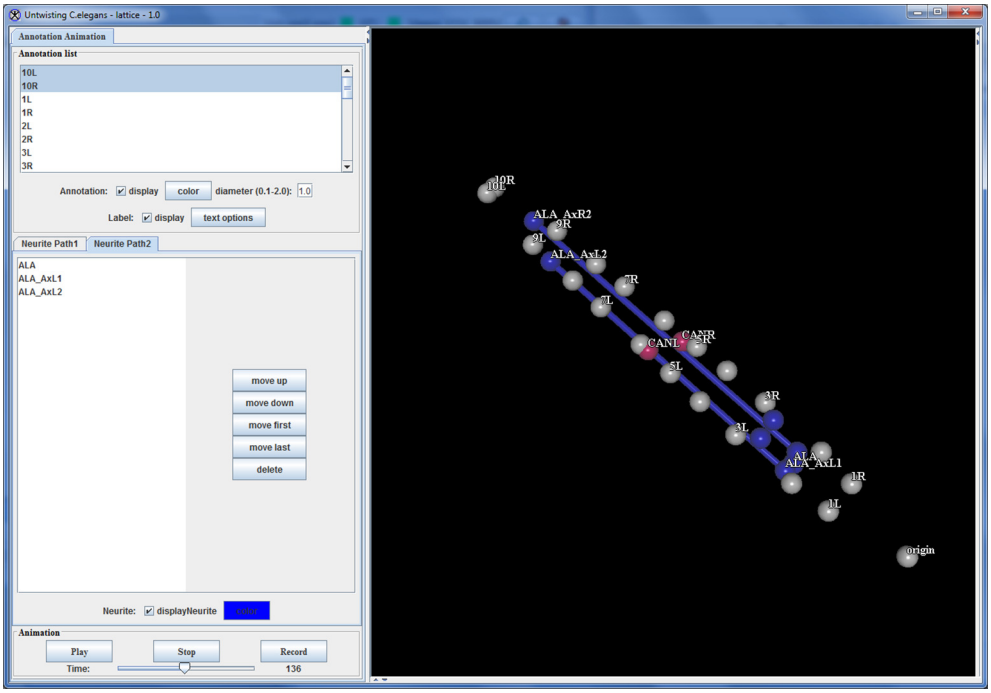

Appendix 1—figure 11. Annotation visualization tool displays changes in positions over time.
DOI: 10.7554/eLife.10070.049

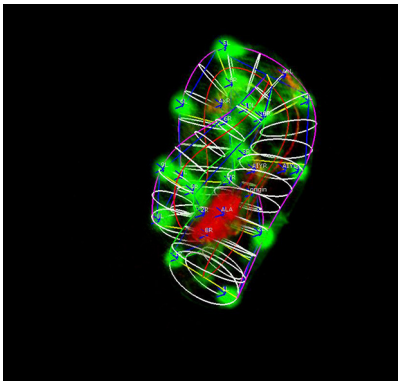

Appendix 1—figure 12. The initial ellipse-based model of the worm. The ellipses fit within the boundaries of the natural spline curves.
DOI: 10.7554/eLife.10070.050

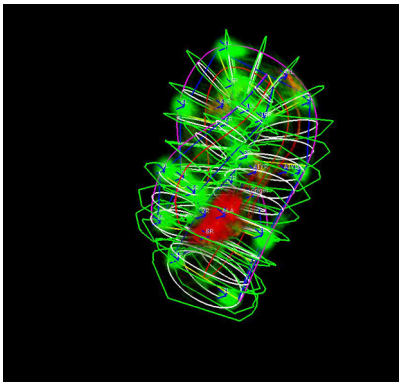

Appendix 1—figure 13. The expanded worm model. The original ellipses are expanded until they contact an adjacent surface of the worm or they reach the boundary of the sample plane.
DOI: 10.7554/eLife.10070.051

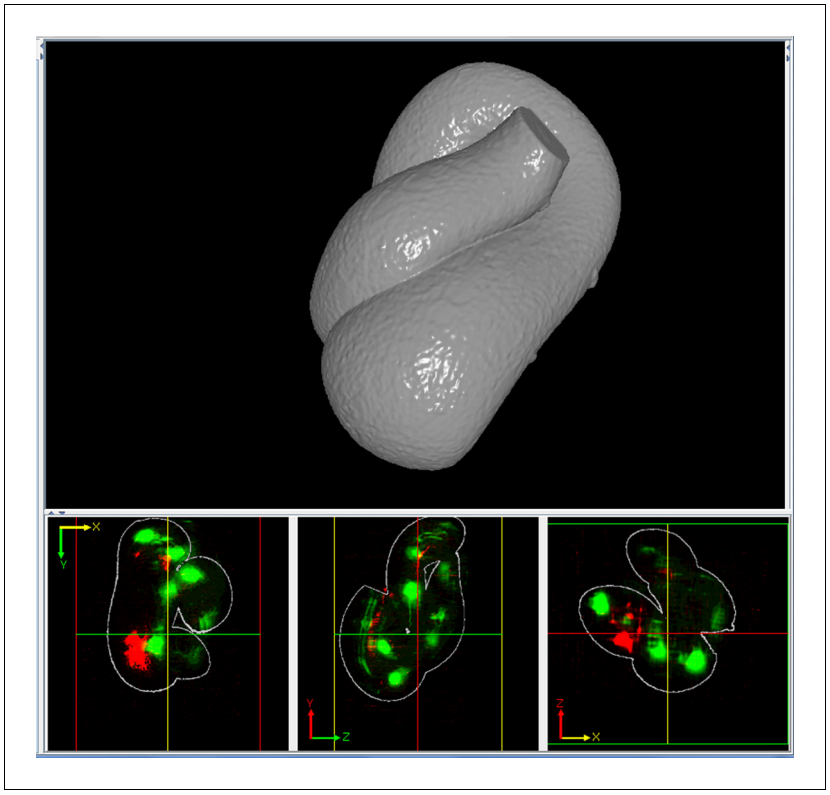

Appendix 1—figure 14. A solid representation of the worm surface. The outlines in the bottom three panels show how the surface encapsulates the volume data.
DOI: 10.7554/eLife.10070.052

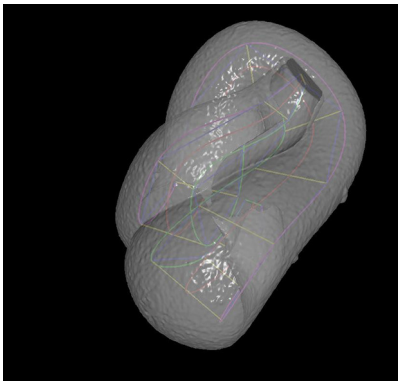

Appendix 1—figure 15. A semi-transparent view of the worm surface model, with the lattice shown inside.
DOI: 10.7554/eLife.10070.053

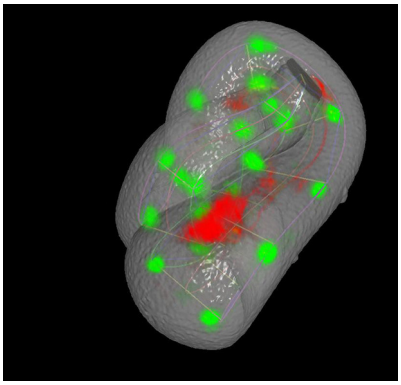

Appendix 1—figure 16. A semi-transparent view of the worm surface model displaying lattice curves, fluorescently- labeled seam cell nuclei, and neuron.
DOI: 10.7554/eLife.10070.054

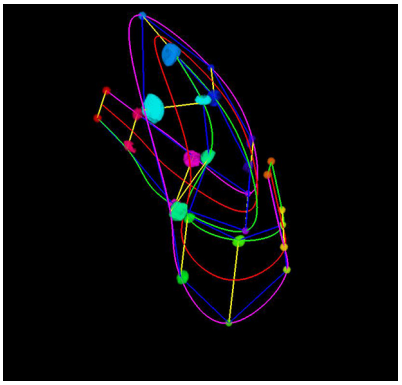

Appendix 1—figure 17. Labeled fluorescent markers. Each pair has a unique color value, indicating which pairs belong on the same slice in the final straightened image. Labeling the lattice pairs this way helps disambiguate voxels with potential conflicts.
DOI: 10.7554/eLife.10070.055

Appendix 1—figure 18. An EM image of the worm shows the worm body is flattened where overlapping segments come into contact.
DOI: 10.7554/eLife.10070.056